SCIENCE CHINA
Mathematics

• ARTICLES •

https://doi.org/10.1007/s11425-020-1748-8

A local discontinuous Galerkin method for pattern formation dynamical model in polymerizing action flocks

Lulu Tian[1], Xiuhui Guo[1], Hui Guo[1,*], Maosheng Jiang[2], Yang Yang[3] & Jiansong Zhang[1]

[1]*College of Science, China University of Petroleum, Qingdao* 266580, *China;*
[2]*Beijing Computational Science Research Center, Beijing* 100193, *China;*
[3]*Department of Mathematics, Michigan Technological University, Houghton, MI* 49931, *USA*

Email: tianll@upc.edu.cn, 1609010130*@s.upc.edu.cn, sdugh@*163*.com, msjiang@csrc.ac.cn, yyang7@mtu.edu, jszhang@upc.edu.cn*

Received March 13, 2020; accepted July 21, 2020

Abstract In this paper, we apply local discontinuous Galerkin methods to the pattern formation dynamical model in polymerizing action flocks. Optimal error estimates for the density and filament polarization in different norms are established. We use a semi-implicit spectral deferred correction time method for time discretization, which allows a relative large time step and avoids computation of a Jacobian matrix. Numerical experiments are presented to verify the theoretical analysis and to show the capability for simulations of action wave formation.

Keywords local discontinuous Galerkin method, error estimate, pattern formation, spectral deferred correction time method

MSC(2010) 65M15, 65M60

Citation: Tian L L, Guo X H, Guo H, et al. A local discontinuous Galerkin method for pattern formation dynamical model in polymerizing action flocks. Sci China Math, 2021, 64, https://doi.org/10.1007/s11425-020-1748-8

1 Introduction

Action filaments are active polymers which stay far from thermodynamic equilibrium. By constantly turning over the components through polymerization and depolymerization, they organize into a variety of states, such as spots, spirals and traveling waves. The mathematical model of the pattern wave for the actin filaments has been investigated intensively [10, 13, 14] in recent days. It is pointed out that the model for wave formation in this paper, proposed in [13], does not require any nonlinear biochemistry and depends on three simple and generic ingredients: actin polymerization, steric repulsion between actin fibers and treadmilling. The numerical experiments in [13] verified the mechanism of the model, where the density was an isotropic low value initially, then raised towards the Onsager threshold. The actin filaments aligned at this state, then destabilized the isotropic phase by actin spots or spirals and finally stayed at a polarized phase.

* Corresponding author

Let Ω be a bounded rectangular domain in $\mathbb{R}^2$. The governing equations of the pattern formation dynamical model in polymerizing action flocks in two space dimensions and in the dimensionless form are as follows [13]:

$$\frac{\partial \rho}{\partial t} = -\nabla \cdot (\rho \boldsymbol{p}) + \nabla^2 \rho + \rho(1-\rho), \quad (x,y) \in \Omega, \quad 0 < t \leqslant T, \tag{1.1}$$

$$\frac{\partial \boldsymbol{p}}{\partial t} = \Gamma\,(r\rho - 1)\,\boldsymbol{p} + \mathcal{D}\nabla^2 \boldsymbol{p} - \Gamma_2 |\boldsymbol{p}|^2 \boldsymbol{p}, \quad (x,y) \in \Omega, \quad 0 < t \leqslant T, \tag{1.2}$$

where ρ and $\boldsymbol{p}$ are the density of action in F-action and the average filament polarization, respectively, $|\boldsymbol{p}|^2 = p_1^2 + p_2^2$ with $\boldsymbol{p} = (p_1, p_2)$, $\Gamma = \gamma/\alpha$, $\mathcal{D} = K/D_\rho$ and $\Gamma_2 = \gamma_2 D_\rho/\nu_0^2$. Here, γ describes the change rate of the direction of F-action filaments and α denotes the polymerization rate. D_ρ and K means the diffusion coefficient and an effective elastic constant, respectively. γ_2 represents saturation of the polarization, and ν_0 is the treadmilling speed.

There are few works discussing numerical simulations for the pattern formation dynamical model. The finite difference method was investigated in [13], and the numerical results verified the idea of the model. Goff et al. [13] showed that Γ has an important impact on waves formation, for example, $\Gamma = 4.3$ and $\Gamma = 10$ generate waves, but $\Gamma = 1$ leads to uniform density. Moreover, spiral shows up at high density spots when $\Gamma = 4.3$ while no spiral emerge for $\Gamma = 10$. Later, characteristic finite element analysis was proposed in [18] for this model and the error estimate was proved under some regularity assumptions of the solution. The time method in the literature [18] used restricted time steps. To the best knowledge of the authors, no previous work focused on discontinuous Galerkin (DG) methods for wave formation. In this paper, we apply the high-order local discontinuous Galerkin (LDG) methods for the pattern formation dynamical model, since the DG method has good stability, high-order accuracy, and flexibility on h-p adaptivity and on complex geometry.

The DG method was first designed in 1973 by Reed and Hill [22] for solving neutron linear transport equations. By using completely discontinuous piecewise polynomials as the numerical solution, the DG method solved hyperbolic conservation laws in a series of papers [4, 6–8] based on the explicit Runge-Kutta time integrations. However, it is difficult to apply the DG method directly to PDEs containing higher-order spatial derivatives. Motivated by Bassi and Rebay [1], Cockburn and Shu [9] introduced the LDG method to solve the convection-diffusion equations. Later on, the LDG method has been successfully designed and applied in many models involving dispersive and higher-order terms [29]. The idea of the LDG method is to rewrite the equation with higher-order derivatives into a first-order system, and then apply the DG method to the system. With suitable numerical fluxes, the stability and optimal error estimates can be proved for many model equations [28, 30, 31]. As an extension of DG schemes for hyperbolic conservation laws, the LDG method results in an extremely local discretization, which offers great advantages in parallel computing and h-p adaptation.

Equations (1.1)–(1.2) contain second-order spacial derivatives, and explicit time methods suffer very small time step sizes. However, to fully recover the pattern formation, we need to set a large final time, say $T = 500$. Therefore, the computational cost would be extremely large. Moreover, the source term in (1.1) modeling pattern formation in actin flocks is important. If the numerical approximation of the density is negative, source would also be negative, leading to even smaller density approximations and even blow-up of the numerical solutions. Therefore, implicit schemes are necessary for the time integrations. In this paper, we present a semi-implicit spectral deferred correction (SDC) time marching method [11, 16, 21, 23] for the pattern formation dynamical model. The SDC time method, as a new variation of the classical deferred correction method, was proposed in [11] to preserve good stability and accuracy for stiff problems. Later, Tang et al. [23] provided a general framework for the convergence of the SDC method. The classical semi-implicit SDC methods have been developed to solve many problems, such as the phase field problems [12, 20] and phase field crystal problems [17]. These semi-implicit time marching methods are mainly efficient for problems with easy separation of stiff and non-stiff components. When it comes to systems not easy to separate the stiff and non-stiff components, traditional semi-implicit schemes are not straightforward to be explored. Recently, a novel semi-implicit SDC time marching method was proposed in [16] for highly nonlinear ODEs without easy separation of stiff and non-stiff components.

The rest of this paper is organized as follows. In Section 2, we present some preliminaries, including assumptions of the solutions of the model, the basic notations and norms to be used throughout the paper and the LDG spatial discretization. Section 3 is the main body of the paper where we present the projections and some essential properties of the finite element spaces, error equations and the details of the optimal error estimates for the pattern formation dynamical model. We provide a semi-implicit spectral deferred correction time integration in Section 4. In Section 5, numerical results are given to demonstrate the accuracy and capability of the LDG-SDC method. We will end in Section 6 with some concluding remarks.

2 Preliminaries

In this section, we demonstrate some preliminary results that will be used throughout the paper.

2.1 Hypotheses for the model

For the pattern formation dynamical model (1.1)–(1.2), the initial conditions are given as

$$\rho(x,y,0)=\rho_0(x,y),\quad \boldsymbol{p}(x,y,0)=\boldsymbol{p}_0(x,y),\quad (x,y)\in\Omega.$$

For simplicity, we consider the periodic boundary condition in this paper. The analysis for homogeneous Neumann boundary can be obtained following the same lines with some minor changes, and we thus omit it.

We make the following hypotheses (H) for the problem:

1. $0<\rho_*\leqslant\rho(x,y,t)\leqslant\rho^*$.
2. Γ, Γ_2, $\mathcal{D}$ and r are all given positive constants.
3. ρ and $\boldsymbol{p}$ are uniformly bounded in $\mathbb{R}^2\times[0,T]$.

2.2 Basic notations

In this subsection, we present the notations. Following [15], let

$$0=x_{\frac{1}{2}}<\cdots<x_{N_x+\frac{1}{2}}=1\quad\text{and}\quad 0=y_{\frac{1}{2}}<\cdots<y_{N_y+\frac{1}{2}}=1$$

be the grid points in the x and y directions, respectively. Define $I_i=(x_{i-\frac{1}{2}},x_{i+\frac{1}{2}})$ and $J_j=(y_{j-\frac{1}{2}},y_{j+\frac{1}{2}})$. Let $K=I_i\times J_j$, $i=1,\ldots,N_x$, $j=1,\ldots,N_y$, be a partition of Ω and denote $\Omega_h=\{K\}$. The mesh sizes in the x and y directions are given as $\Delta x_i=x_{i+\frac{1}{2}}-x_{i-\frac{1}{2}}$ and $\Delta y_j=y_{j+\frac{1}{2}}-y_{j-\frac{1}{2}}$, respectively and

$$h=\max\Big\{\max_i\Delta x_i,\max_j\Delta y_j\Big\}.$$

Moreover, we assume the partition is quasi-uniform, i.e., there exists a positive constant λ such that $h\leqslant\lambda h_{\min}$, where

$$h_{\min}=\min\Big\{\min_i\Delta x_i,\min_j\Delta y_j\Big\}.$$

Associated with this mesh, we define the finite element space as

$$W_h^k=\{z\in L^2(\Omega):z\,|_K\in Q^k(K),\,\forall\,K\in\Omega_h\},$$

where $Q^k(K)$ denotes the space of tensor product polynomials of degrees at most k in K. Finite element spaces for the vector and the matrix are defined as

$$\begin{aligned}&\underline{U}_h=\{\underline{u}\in L^2(\Omega)^{2\times2}:\underline{u}\,|_K\in Q_k(K)^{2\times2},\,\forall\,K\in\Omega_h\},\\&\boldsymbol{W}_h=\{\boldsymbol{w}\in L^2(\Omega)^2:\boldsymbol{w}\,|_K\in Q_k(K)^2,\,\forall\,K\in\Omega_h\},\\&V_h=W_h^k,\end{aligned}$$

which is contained in the following mesh-dependent broken Sobolev space $\underline{\boldsymbol{U}} \times \boldsymbol{W} \times V$:

$$\begin{aligned}
&\underline{U} = \{\underline{u} \in L^2(\Omega)^{2\times 2} : \underline{u}\,|_K \in H^1(K)^{2\times 2}, \forall\, K \in \Omega_h\},\\
&\boldsymbol{W} = \{\boldsymbol{w} \in L^2(\Omega)^2 : \boldsymbol{w}\,|_K \in H^1(K)^2, \forall\, K \in \Omega_h\},\\
&V = \{v \in L^2(\Omega) : v\,|_K \in H^1(K), \forall\, K \in \Omega_h\},
\end{aligned}$$

respectively. $Q^k(K)$ denotes the space of tensor product polynomials of degrees at most k in K. We choose $\boldsymbol{\beta} = (1,1)^{\mathrm{T}}$ to be a fixed vector that is not parallel to any normals of the element interfaces. We denote Γ_h to be the set of all element interfaces and $\Gamma_0 = \Gamma_h \backslash \partial\Omega$. Let $\mathcal{E} \in \Gamma_0$ be an interior edge shared by the elements K_ℓ and K_r, where $\boldsymbol{\beta}\cdot\boldsymbol{n}_\ell > 0$ and $\boldsymbol{\beta}\cdot\boldsymbol{n}_r < 0$ with $\boldsymbol{n}_\ell$ and $\boldsymbol{n}_r$ being the outward normals of K_ℓ and K_r, respectively. For any $z \in V_h$, we define $z^- = z\,|_{\partial K_\ell}$ and $z^+ = z\,|_{\partial K_r}$, respectively. The jump is given as $[z] = z^+ - z^-$. Moreover, for $\boldsymbol{p} \in \boldsymbol{W}_h$ and $\underline{u} \in \underline{U}_h$, we can define $\boldsymbol{p}^+$, $\underline{u}^+$, $\boldsymbol{p}^-$, $\underline{u}^-$ and $[\boldsymbol{p}]$, $[\underline{u}]$ analogously. We also define $\partial\Omega_- = \{\mathcal{E} \in \partial\Omega \mid \boldsymbol{\beta}\cdot\boldsymbol{n} < 0\}$, where $\boldsymbol{n}$ is the outer normal of $\mathcal{E}$, and $\partial\Omega_+ = \partial\Omega\backslash\partial\Omega_-$. For any $\mathcal{E} \in \partial\Omega_-$, there exists $K \in \Omega_h$ such that $\mathcal{E} \in \partial K$, we define $z^+\,|_{\mathcal{E}} = z\,|_{\partial K}$, and define z^- on $\partial\Omega_+$ analogously. For simplicity, given $\mathcal{E} = \{x_{\frac{1}{2}}\} \times J_j \in \partial\Omega_-$ and $\tilde{\mathcal{E}} = \{x_{N_x+\frac{1}{2}}\} \times J_j \in \partial\Omega_+$, by the periodic boundary condition, we define

$$z^-\,|_{\mathcal{E}} = z^-\,|_{\tilde{\mathcal{E}}} \quad \text{and} \quad z^+\,|_{\tilde{\mathcal{E}}} = z^+\,|_{\mathcal{E}}.$$

Similarly, given $\mathcal{E} = I_i \times \{y_{\frac{1}{2}}\} \in \partial\Omega_-$ and $\tilde{\mathcal{E}} = I_i \times \{y_{N_y+\frac{1}{2}}\} \in \partial\Omega_+$, we define

$$z^-\,|_{\mathcal{E}} = z^-\,|_{\tilde{\mathcal{E}}} \quad \text{and} \quad z^+\,|_{\tilde{\mathcal{E}}} = z^+\,|_{\mathcal{E}}.$$

Throughout this paper, the symbol C is used as a generic constant which may appear differently at different occurrences. Moreover, the symbol ϵ is a sufficiently small positive constant.

2.3 Norms

In this subsection, we define several norms that will be used throughout the paper. For any given domain $D \subset \mathbb{R}^d$, $d = 2$, we denote by $\|v\|_D$ the L^2 norm of v on D. For any integer $s \geqslant 0$, let $H^s(D)$ represent the space equipped with the norm $\|\cdot\|_{s,D}$, in which the function itself and the derivatives up to the s-th-order are all in $L^2(D)$. Similar norms for the vector-valued function $\boldsymbol{w}$ and the matrix-valued function $\underline{u}$ can be defined in a similar way, given by

$$\|\boldsymbol{w}\|_{s,D} = \Big(\sum_{i=1}^{d} \|w_i\|_{s,D}^2\Big)^{1/2} \quad \text{and} \quad \|\underline{u}\|_{s,D} = \Big(\sum_{i,j=1}^{d} \|u_{ij}\|_{s,D}^2\Big)^{1/2},$$

respectively. We also define

$$\|\boldsymbol{w}\|_{\Gamma_h} = \Big(\sum_{e\in\Gamma_h} \|\boldsymbol{w}\|_e^2\Big)^{1/2}, \quad \|\underline{u}\|_{\Gamma_h} = \Big(\sum_{e\in\Gamma_h} \|\underline{u}\|_e^2\Big)^{1/2} \quad \text{and} \quad \|\nabla\boldsymbol{w}\| = \Big(\sum_{K\in\Omega_h} \|\nabla\boldsymbol{w}\|_K^2\Big)^{1/2}$$

for $\boldsymbol{w} \in \boldsymbol{W}_h$.

Denote $\|u\|_{0,K}$ to be the standard L^2 norm of u in the cell K. For any natural number ℓ, we consider the norm of the Sobolev space $H^\ell(K)$, defined by

$$\|u\|_{\ell,K} = \Big\{\sum_{0\leqslant\alpha+\beta\leqslant\ell} \Big\|\frac{\partial^{\alpha+\beta}u}{\partial x^\alpha \partial y^\beta}\Big\|_{0,K}^2\Big\}^{\frac{1}{2}}.$$

Moreover, we define the norms on the whole computational domain as

$$\|u\|_\ell = \Big(\sum_{K\in\Omega_h} \|u\|_{\ell,K}^2\Big)^{\frac{1}{2}}.$$

For convenience, if we consider the standard L^2 norm, then the corresponding subscript will be omitted.

Let Γ_K be the edges of K, and we define

$$\|u\|^2_{\Gamma_K} = \int_{\partial K} u^2 ds.$$

We also define

$$\|u\|^2_{\Gamma_h} = \sum_{K\in\Omega_h} \|u\|^2_{\Gamma_K}.$$

Moreover, we define the standard L^∞ norm of u in K as $\|u\|_{\infty,K}$, and define the L^∞ norm on the whole computational domain as

$$\|u\|_\infty = \max_{K\in\Omega_h} \|u\|_{\infty,K}.$$

Finally, we define similar norms for the vector $\boldsymbol{u} = (u_1, u_2)^{\mathrm{T}}$ as

$$\|\boldsymbol{u}\|^2_{\ell,K} = \|u_1\|^2_{\ell,K} + \|u_2\|^2_{\ell,K}, \quad \|\boldsymbol{u}\|^2_{\Gamma_K} = \|u_1\|^2_{\Gamma_K} + \|u_2\|^2_{\Gamma_K}, \quad \|\boldsymbol{u}\|_{\infty,K} = \max\{\|u_1\|_{\infty,K}, \|u_2\|_{\infty,K}\}.$$

Similarly, the norms on the whole computational domain are given as

$$\|\boldsymbol{u}\|^2_\ell = \sum_{K\in\Omega_h} \|\boldsymbol{u}\|^2_{\ell,K}, \quad \|\boldsymbol{u}\|^2_{\Gamma_h} = \sum_{K\in\Omega_h} \|\boldsymbol{u}\|^2_{\Gamma_K}, \quad \|\boldsymbol{u}\|_\infty = \max_{K\in\Omega_h} \|\boldsymbol{u}\|_{\infty,K}.$$

The inner products of two functions in the finite element spaces $V_h, \boldsymbol{W}_h$ and $\underline{U}$ on the element K are defined as

$$(u, v)_K = \int_K uv dxdy, \quad (\boldsymbol{u}, \boldsymbol{v})_K = \int_K \boldsymbol{u}\cdot\boldsymbol{v} dxdy, \quad (\underline{u}, \underline{v})_K = \int_K \underline{u} : \underline{v} dxdy.$$

2.4 The LDG scheme

In this subsection, we devise an LDG scheme for the dynamic model of pattern formation. By introducing some auxiliary variables to represent the derivatives of the solution, the nonlinear system (1.1)–(1.2) can be rewritten as the following first-order system:

$$\frac{\partial \rho}{\partial t} + \nabla\cdot(\rho\boldsymbol{p}) + \nabla\cdot\boldsymbol{s} = \rho(1-\rho), \tag{2.1}$$

$$\boldsymbol{s} + \nabla\rho = \boldsymbol{0}, \tag{2.2}$$

$$\frac{\partial \boldsymbol{p}}{\partial t} + \nabla\cdot\underline{u} - \Gamma(r\rho - 1)\boldsymbol{p} + \Gamma_2|\boldsymbol{p}|^2\boldsymbol{p} = 0, \tag{2.3}$$

$$\frac{1}{\mathcal{D}}\underline{u} = -\nabla\boldsymbol{p}. \tag{2.4}$$

The notations in this paper are the same as those in [5, 25]. Suppose $\partial_1\cdot = \partial_x\cdot$ and $\partial_2\cdot = \partial_y\cdot$. Then the gradient of the vector $\boldsymbol{p}$ is a matrix with $(\nabla\boldsymbol{p})_{ij} = \partial_j\boldsymbol{p}_i$. The divergence of the matrix $\underline{u}$ is a vector with

$$(\nabla\cdot\underline{u})_i = \sum_{j=1}^{d} \partial_j \underline{u}_{ij}.$$

We also define, for any $\boldsymbol{\theta}, \boldsymbol{n} \in \boldsymbol{W}_h$ and $\underline{u}, \underline{r} \in \underline{U}_h$,

$$\underline{u} : \underline{r} = \sum_{i,j=1}^{d} \underline{u}_{ij}\underline{r}_{ij}, \quad \boldsymbol{\theta}\cdot\underline{u}\cdot\boldsymbol{n} = \sum_{i,j=1}^{d} \boldsymbol{\theta}_i\underline{u}_{ij}n_j.$$

The LDG scheme for the first-order system (2.1)–(2.4) is to find the approximation

$$(\rho_h, \boldsymbol{s}_h, \boldsymbol{p}_h, \underline{u}_h) \in V_h \times \boldsymbol{W}_h \times \boldsymbol{W}_h \times \underline{U}_h,$$

such that the following variation forms hold for any element $K \in \Omega_h$, and any test functions $v,\ \boldsymbol{w},\ \boldsymbol{\theta},\ \underline{r} \in V_h \times \boldsymbol{W}_h \times \boldsymbol{W}_h \times \underline{U}_h$:

$$\int_K \frac{\partial \rho_h}{\partial t} v dxdy = \mathcal{Q}_K^{\rho}(\boldsymbol{p}_h, \rho_h; v) + \mathcal{Q}_K(\boldsymbol{s}_h, v) + \int_K \rho_h(1-\rho_h) v dxdy, \tag{2.5}$$

$$\int_K \boldsymbol{s}_h \cdot \boldsymbol{w} dxdy = \mathcal{P}_K(\rho_h, \boldsymbol{w}), \tag{2.6}$$

$$\int_K \frac{\partial \boldsymbol{p}_h}{\partial t} \cdot \boldsymbol{\theta} dxdy = \mathcal{L}_K(\underline{u}_h, \boldsymbol{\theta}) + \int_K (\Gamma(r\rho_h - 1)\boldsymbol{p}_h - \Gamma_2 |\boldsymbol{p}_h|^2 \boldsymbol{p}_h) \cdot \boldsymbol{\theta} dxdy, \tag{2.7}$$

$$\int_K \frac{1}{\mathcal{D}} \underline{u}_h : \underline{r} dxdy = \mathcal{K}_K(\boldsymbol{p}_h, \underline{r}). \tag{2.8}$$

Here,

$$\mathcal{Q}_K^{\rho}(\boldsymbol{p}_h, \rho_h; v) = \int_K \rho_h \boldsymbol{p}_h \cdot \nabla v dxdy - \int_{\partial K} \widehat{\rho_h \boldsymbol{p}_h} \cdot \ \boldsymbol{n}_K v ds, \tag{2.9}$$

$$\mathcal{Q}_K(\boldsymbol{s}_h, v) = \int_K \boldsymbol{s}_h \cdot \nabla v dxdy - \int_{\partial K} \widehat{\boldsymbol{s}_h} \cdot \boldsymbol{n}_K v ds, \tag{2.10}$$

$$\mathcal{P}_K(\rho_h, \boldsymbol{w}) = \int_K \rho_h \nabla \cdot \boldsymbol{w} dxdy - \int_{\partial K} \widehat{\rho_h} \boldsymbol{w} \cdot \boldsymbol{n}_K ds, \tag{2.11}$$

$$\mathcal{L}_K(\underline{u}_h, \boldsymbol{\theta}) = \int_K \underline{u}_h : \nabla \boldsymbol{\theta} dxdy - \int_{\partial K} \boldsymbol{\theta} \cdot \widehat{\underline{u}_h} \cdot \boldsymbol{n}_K ds, \tag{2.12}$$

$$\mathcal{K}_K(\boldsymbol{p}_h, \underline{r}) = \int_K \boldsymbol{p}_h \cdot \nabla \cdot \underline{r} dxdy - \int_{\partial K} \widehat{\boldsymbol{p}_h} \cdot \underline{r} \cdot \boldsymbol{n}_K ds. \tag{2.13}$$

The "hat" terms are the so-called numerical flux. We use alternating fluxes for the diffusion term and take

$$\widehat{\boldsymbol{s}_h} = \boldsymbol{s}_h^+, \quad \widehat{\rho_h} = \rho_h^-, \tag{2.14}$$

$$\widehat{\underline{u}_h} = \underline{u}_h^+, \quad \widehat{\boldsymbol{p}_h} = \boldsymbol{p}_h^-. \tag{2.15}$$

For the convection term, we take

$$\widehat{\rho_h \boldsymbol{p}_h} = \frac{1}{2}(\rho_h^+ \boldsymbol{p}_h^+ + \rho_h^- \boldsymbol{p}_h^- - \alpha \boldsymbol{n}_e(\rho_h^+ - \rho_h^-)),$$

where $\alpha \geqslant 0$ can be chosen as any fixed constant independent of h and $\boldsymbol{n}_e$ is the unit normal of $e \in \Gamma_0$ such that $\boldsymbol{\beta} \cdot \boldsymbol{n}_e > 0$.

2.5 Useful projections

Suppose that P^k denotes the space of polynomials of degrees no more than k. We will use several special projections in this paper. Firstly, we define π^+ into W_h^k which is, for each cell K,

$$(\pi^+ u - u, v)_K = 0, \quad \forall\, v \in Q^{k-1}(K), \quad \int_{J_j} (\pi^+ u - u)(x_{i-\frac{1}{2}}, y) v(y) dy = 0, \quad \forall\, v \in P^{k-1}(J_j),$$

$$\int_{I_i} (\pi^+ u - u)(x, y_{j-\frac{1}{2}}) v(x) dx = 0, \quad \forall\, v \in P^{k-1}(I_i), \quad (\pi^+ u - u)(x_{i-\frac{1}{2}}, y_{j-\frac{1}{2}}) = 0, \quad \forall\, i, \forall\, j,$$

and in the same way for π^-,

$$(\pi^- u - u, v)_K = 0, \quad \forall\, v \in Q^{k-1}(K), \quad \int_{J_j} (\pi^- u - u)(x_{i+\frac{1}{2}}, y) v(y) dy = 0, \quad \forall\, v \in P^{k-1}(J_j),$$

$$\int_{I_i} (\pi^- u - u)(x, y_{j+\frac{1}{2}}) v(x) dx = 0, \quad \forall\, v \in P^{k-1}(I_i), \quad (\pi^- u - u)(x_{i+\frac{1}{2}}, y_{j+\frac{1}{2}}) = 0, \quad \forall\, i, \forall\, j.$$

Subsequently, we define Π_x^+ and Π_y^+ into W_h^k which are, for each cell K,

$$\begin{aligned}
&(\Pi_x^+ u - u, v_x)_K = 0, \quad \forall\, v \in Q^k(K),\\
&\int_{J_j} (\Pi_x^+ u - u)(x_{i-\frac{1}{2}}, y) v(y) dy = 0, \quad \forall\, v \in P^k(J_j),\\
&(\Pi_y^+ u - u, v_y)_K = 0, \quad \forall\, v \in Q^k(K),\\
&\int_{I_i} (\Pi_y^+ u - u)(x, y_{j-\frac{1}{2}}) v(x) dx = 0, \quad \forall\, v \in P^k(I_i),
\end{aligned}$$

as well as a vector-valued projection

$$\boldsymbol{\Pi}^+ \begin{pmatrix} s_1 \\ s_2 \end{pmatrix} = \begin{pmatrix} \Pi_x^+ s_1 \\ \Pi_y^+ s_2 \end{pmatrix}.$$

We define the projections $\underline{\Pi}^+, \boldsymbol{\pi}^+$ and $\boldsymbol{\pi}^-$ based on the projections defined above. For the vector-valued function $\boldsymbol{p} = (p_1, p_2)^{\mathrm{T}} \in \boldsymbol{W}$, we define

$$\boldsymbol{\pi}^- \boldsymbol{p} = (\pi^- p_1, \pi^- p_2)^{\mathrm{T}}.$$

For the matrix-valued function $\underline{u} = (\boldsymbol{u}_1, \boldsymbol{u}_2) \in \underline{U}$, where $\boldsymbol{u}_1$ and $\boldsymbol{u}_2$ are its two column vectors, we define

$$\underline{\Pi}^+ \underline{u} = (\boldsymbol{\Pi}^+ \boldsymbol{u}_1, \boldsymbol{\Pi}^+ \boldsymbol{u}_2).$$

We choose the initial solution as

$$\rho_h(x, y, 0) = \pi^- \rho_0, \quad \boldsymbol{p}_h(x, y, 0) = \boldsymbol{\pi}^- \boldsymbol{p}_0, \tag{2.16}$$

and then we have

$$\|\rho(x, y, 0) - \rho_h(x, y, 0)\| \leqslant C h^{k+1}, \quad \|\boldsymbol{p}(x, y, 0) - \boldsymbol{p}_h(x, y, 0)\| \leqslant C h^{k+1}.$$

Moreover, we define

$$\begin{aligned}
&(u, v) = \sum_{K \in \Omega_h} (u, v)_K, \quad (\boldsymbol{u}, \boldsymbol{v}) = \sum_{K \in \Omega_h} (\boldsymbol{u}, \boldsymbol{v})_K, \quad (\underline{u}, \underline{v}) = \sum_{K \in \Omega_h} (\underline{u}, \underline{v})_K,\\
&\mathcal{Q}^\rho(\boldsymbol{p}, \rho; v) = \sum_{K \in \Omega_h} \mathcal{Q}_K^\rho(\boldsymbol{p}, \rho; v), \quad \Xi(\cdot, \cdot) = \sum_{K \in \Omega_h} \Xi_K(\cdot, \cdot)
\end{aligned} \tag{2.17}$$

with $\Xi = \mathcal{Q}, \mathcal{P}, \mathcal{L}, \mathcal{K}$.

It is easy to check the following identity by integration by parts on each cell.

Lemma 2.1. *For any functions $(v, \boldsymbol{p}, \boldsymbol{s}, \underline{u}) \in V_h \times \boldsymbol{W}_h \times \boldsymbol{W}_h \times \underline{U}_h$, we have*

$$\mathcal{L}(\underline{u}, \boldsymbol{p}) + \mathcal{K}(\boldsymbol{p}, \underline{u}) = 0, \quad \mathcal{Q}(\boldsymbol{s}, \rho) + \mathcal{P}(\rho, \boldsymbol{s}) = 0. \tag{2.18}$$

Now we state the main theorem.

Theorem 2.2. *Let $\rho_h, \boldsymbol{p}_h, \boldsymbol{s}_h$ and $\underline{u}_h$ be the numerical solutions of the semi-discrete LDG scheme* (2.5)–(2.8) *with initial discretization given as* (2.16)*, and let $\rho \in L^\infty(0, T; H^{k+3})$, $\boldsymbol{s} \in L^\infty(0, T; (H^{k+2})^2)$, $\underline{u} \in L^\infty(0, T; (H^{k+2})^{2\times 2})$ and $\boldsymbol{p} \in L^\infty(0, T; (H^{k+3})^2)$ be the exact solutions of the problem* (2.1)–(2.4)*. If the finite element space is the piecewise tensor product polynomials of degrees at most k and h is sufficiently small, then we have the error estimate*

$$\|\rho - \rho_h\|_{L^\infty(0,T;L^2)} + \|\boldsymbol{p} - \boldsymbol{p}_h\|_{L^\infty(0,T;L^2)} + \|\boldsymbol{s} - \boldsymbol{s}_h\|_{L^2(0,T;L^2)} + \|\underline{u} - \underline{u}_h\|_{L^2(0,T;L^2)} \leqslant C h^{k+1}, \tag{2.19}$$

where the constant C is independent of h.

3 Proof of the main theorem

In this section, we proceed to prove Theorem 2.2. We first introduce some auxiliary results for the projections defined in Section 2. Subsequently, we make an *a priori* error estimate which provides the boundedness of the numerical approximations. Then we construct the error equations which further yield several main energy inequalities and complete the proof of (2.19). Finally, we verify the *a priori* error estimate at the end of this section.

3.1 Projections and interpolation properties

In this section, we demonstrate the projections and several useful lemmas. Let us start with the classical inverse properties [3].

Lemma 3.1. *Assume $u \in V_h$. Then there exists a positive constant C independent of h and u such that*

$$h\|u\|_{\infty,K} + h^{1/2}\|u\|_{\Gamma_K} \leqslant C\|u\|_K.$$

Lemma 3.2. *Suppose $w \in H^{k+1}(\Omega)$. Then for any projection P_h, which is either π^-, Π_x^+ or Π_y^+, we have*

$$\|w - P_h w\| + h^{1/2}\|w - P_h w\|_{\Gamma_h} \leqslant Ch^{k+1}.$$

Moreover, the projection π^- on the Cartesian meshes has the following superconvergence property [2].

Lemma 3.3. *Suppose $\rho \in H^{k+2}(\Omega)$. Then for any $\boldsymbol{s} \in \boldsymbol{W}_h$, we have*

$$|\mathcal{P}(\rho - \pi^-\rho, \boldsymbol{s})| \leqslant Ch^{k+1}\|\rho\|_{k+2}\|\boldsymbol{s}\|. \tag{3.1}$$

In this paper, we use e to denote the error between the exact and numerical solutions, i.e.,

$$\underline{e}_{\underline{u}} = \underline{u} - \underline{u}_h, \quad e_\rho = \rho - \rho_h, \quad \boldsymbol{e_p} = \boldsymbol{p} - \boldsymbol{p}_h, \quad \boldsymbol{e_s} = \boldsymbol{s} - \boldsymbol{s}_h.$$

As the general treatment of the finite element methods, we split the errors into two terms as

$$\begin{aligned}
&e_\rho = \xi_\rho - \eta_\rho, \quad \eta_\rho = \pi^-\rho - \rho, \quad \xi_\rho = \pi^-\rho - \rho_h,\\
&\boldsymbol{e_p} = \boldsymbol{\xi_p} - \boldsymbol{\eta_p}, \quad \boldsymbol{\eta_p} = \boldsymbol{\pi}^-\boldsymbol{p} - \boldsymbol{p}, \quad \boldsymbol{\xi_p} = \boldsymbol{\pi}^-\boldsymbol{p} - \boldsymbol{p}_h,\\
&\boldsymbol{e_s} = \boldsymbol{\xi_s} - \boldsymbol{\eta_s}, \quad \boldsymbol{\eta_s} = \Pi^+\boldsymbol{s} - \boldsymbol{s}, \quad \boldsymbol{\xi_s} = \Pi^+\boldsymbol{s} - \boldsymbol{s}_h,\\
&\underline{e}_{\underline{u}} = \underline{\xi}_{\underline{u}} - \underline{\eta}_{\underline{u}}, \quad \underline{\eta}_{\underline{u}} = \underline{\Pi}^+\underline{u} - \underline{u}, \quad \underline{\xi}_{\underline{u}} = \underline{\Pi}^+\underline{u} - \underline{u}_h.
\end{aligned}$$

Based on the above notations, it is easy to verify that

$$\mathcal{L}(\underline{\eta}_{\underline{u}}, v) = 0, \quad \mathcal{Q}(\boldsymbol{\eta_s}, v) = 0, \quad \forall\, v \in Q^k(K). \tag{3.2}$$

Following [24, 26, 27, 32] with some minor changes, we have the following lemma.

Lemma 3.4. *Suppose that ξ_ρ and $\boldsymbol{\xi_s}$ are defined above. We have*

$$\|\nabla\xi_\rho\| \leqslant C(\|\boldsymbol{\xi_s}\| + h^{k+1}), \quad h^{-\frac{1}{2}}\|[\xi_\rho]\|_{\Gamma_h} \leqslant C(\|\boldsymbol{\xi_s}\| + h^{k+1}).$$

Let us finish this subsection by proving the following lemma whose proof was given in [19].

Lemma 3.5. *Let $u \in C^{k+1}(\Omega)$ and $\Pi u \in W_h^k$. Suppose $\|u - \Pi u\| \leqslant Ch^\kappa$ for some positive constant C and $\kappa \leqslant k+1$. Then*

$$h\|u - \Pi u\|_\infty + h^{1/2}\|u - \Pi u\|_{\Gamma_h} \leqslant Ch^\kappa,$$

where the positive constant C does not depend on h.

3.2 The *a priori* error estimate

In this subsection, we make an *a priori* error estimate assumption that

$$\|\rho - \rho_h\| + \|\boldsymbol{p} - \boldsymbol{p}_h\| \leqslant h, \tag{3.3}$$

which further implies

$$\|\rho_h\|_\infty + \|\boldsymbol{p}_h\|_\infty \leqslant C \tag{3.4}$$

by Lemma 3.5.

Remark 3.6. The *a priori* estimate assumption (3.3) holds for small enough h and this choice is heavily based on how large the constant C is in (2.19). Notice that the constant C is independent of h, as long as h is sufficiently small, say $h < H$. Then we can guarantee (3.3) holds for $0 \leqslant t \leqslant T$. Moreover, we will show that, if $h < H$, then the equality of (3.3) cannot happen if $t < T$. However, we still need this estimate to obtain the boundedness of the numerical approximations. This assumption, which will be verified in Subsection 3.6, is used for the estimate of the convection terms.

3.3 Error equations

In this subsection, we proceed to construct the error equations. From (2.5)–(2.8), we have the following error equations:

$$\left(\frac{\partial e_\rho}{\partial t}, v\right) = \mathcal{Q}^\rho(\boldsymbol{p}, \rho; v) - \mathcal{Q}^\rho(\boldsymbol{p}_h, \rho_h; v) + \mathcal{Q}(\boldsymbol{e_s}, v) + (\rho(1-\rho) - \rho_h(1-\rho_h), v), \tag{3.5}$$

$$(\boldsymbol{e_s}, \boldsymbol{w}) = \mathcal{P}(e_\rho, \boldsymbol{w}), \tag{3.6}$$

$$\left(\frac{\partial \boldsymbol{e_p}}{\partial t}, \boldsymbol{\theta}\right) = \mathcal{L}(\underline{e_u}, \boldsymbol{\theta}) + \Gamma((r\rho - 1)\boldsymbol{p} - (r\rho_h - 1)\boldsymbol{p}_h, \boldsymbol{\theta}) - \Gamma_2(|\boldsymbol{p}|^2\boldsymbol{p} - |\boldsymbol{p}_h|^2\boldsymbol{p}_h, \boldsymbol{\theta}), \tag{3.7}$$

$$\frac{1}{\mathcal{D}}(\underline{e_u}, \underline{r}) = \mathcal{K}(\boldsymbol{e_p}, \underline{r}) \tag{3.8}$$

for any $v \in V_h$, $\boldsymbol{w}, \boldsymbol{\theta} \in \boldsymbol{W}_h$ and $\underline{r} \in \underline{U}_h$.

3.4 The first energy inequality

In this subsection, we will derive the first energy inequality. Taking $v = \xi_\rho$, $\boldsymbol{w} = \boldsymbol{\xi_s}$ in (3.5) and (3.6), respectively, and using Lemma 2.1, we can obtain

$$\left(\frac{\partial \xi_\rho}{\partial t}, \xi_\rho\right) + (\boldsymbol{\xi}_s, \boldsymbol{\xi}_s) =: R_1 + R_2 + R_3 + R_4, \tag{3.9}$$

where

$$\begin{aligned}
R_1 &:= \left(\frac{\partial \eta_\rho}{\partial t}, \xi_\rho\right) + (\boldsymbol{\eta_s}, \boldsymbol{\xi_s}),\\
R_2 &:= (\rho\boldsymbol{p} - \rho_h\boldsymbol{p}_h, \nabla\xi_\rho) + \sum_{e\in\Gamma_e} \langle(\rho\boldsymbol{p} - \widehat{\rho_h\boldsymbol{p}_h})\cdot\boldsymbol{n}_e, [\xi_\rho]\rangle_e,\\
R_3 &:= (\rho(1-\rho) - \rho_h(1-\rho_h), \xi_\rho),\\
R_4 &:= -\mathcal{P}(\eta_\rho, \boldsymbol{\xi_s})
\end{aligned}$$

with $\Gamma_e = \Gamma_0 \cup \partial\Omega_-$ and $\langle u, v\rangle_e = \int_e uv\, ds$. Now, we estimate R_i $(i = 1, \ldots, 4)$ term by term. Using the Schwarz inequality and Lemma 3.2, we can get

$$\begin{aligned}
R_1 &\leqslant C\|\eta_{\rho_t}\|\|\xi_\rho\| + C\|\boldsymbol{\eta_s}\|\|\boldsymbol{\xi_s}\|\\
&\leqslant Ch^{k+1}(\|\xi_\rho\| + \|\boldsymbol{\xi_s}\|) \leqslant Ch^{2k+2} + \|\xi_\rho\|^2 + \epsilon\|\boldsymbol{\xi_s}\|^2.
\end{aligned} \tag{3.10}$$

We estimate R_2 by dividing it into three parts

$$R_2 =: R_{21} + R_{22} - R_{23}, \tag{3.11}$$

where

$$\begin{aligned}
R_{21} &= (\rho\boldsymbol{p} - \rho_h\boldsymbol{p}, \nabla\xi_\rho) + (\rho_h\boldsymbol{p} - \rho_h\boldsymbol{p}_h, \nabla\xi_\rho),\\
R_{22} &= \frac{1}{2}\sum_{e\in\Gamma_e}\langle(2\rho\boldsymbol{p} - \rho_h^+\boldsymbol{p}_h^+ - \rho_h^-\boldsymbol{p}_h^-)\cdot\boldsymbol{n}_e, [\xi_\rho]\rangle_e,\\
R_{23} &= \frac{1}{2}\sum_{e\in\Gamma_e}\langle\alpha[\xi_\rho - \eta_\rho], [\xi_\rho]\rangle_e.
\end{aligned}$$

Using Hypothesis 3 and (3.4), we have

$$\begin{aligned}
R_{21} &\leqslant C(\|\rho - \rho_h\| + \|\boldsymbol{p} - \boldsymbol{p}_h\|)\|\nabla\xi_\rho\|\\
&\leqslant C(h^{k+1} + \|\xi_\rho\| + \|\boldsymbol{\xi_p}\|)(\|\boldsymbol{\xi_s}\| + h^{k+1})\\
&\leqslant C(h^{2k+2} + \|\xi_\rho\|^2 + \|\boldsymbol{\xi_p}\|^2) + \epsilon\|\boldsymbol{\xi_s}\|^2,
\end{aligned} \tag{3.12}$$

where in the first step we use the Schwarz inequality while the second step follows from Lemmas 3.2 and 3.4. C depends on $\|\boldsymbol{p}\|_\infty$ and $\|\rho_h\|_\infty$. The estimate of R_{22} also requires Hypothesis 3 and (3.4),

$$\begin{aligned}
R_{22} &= \frac{1}{2}\sum_{e\in\Gamma_e}\langle(\boldsymbol{p}(\rho - \rho_h^+) + (\boldsymbol{p} - \boldsymbol{p}_h^+)\rho_h^+ + \boldsymbol{p}(\rho - \rho_h^-) + (\boldsymbol{p} - \boldsymbol{p}_h^-)\rho_h^-)\cdot\boldsymbol{n}_e, [\xi_\rho]\rangle_e\\
&\leqslant C(\|\rho - \rho_h\|_{\Gamma_h} + \|\boldsymbol{p} - \boldsymbol{p}_h\|_{\Gamma_h})\|[\xi_\rho]\|_{\Gamma_h}\\
&\leqslant Ch^{\frac{1}{2}}(\|\eta_\rho\|_{\Gamma_h} + \|\xi_\rho\|_{\Gamma_h} + \|\boldsymbol{\eta_p}\|_{\Gamma_h} + \|\boldsymbol{\xi_p}\|_{\Gamma_h})(\|\boldsymbol{\xi_s}\| + h^{k+1})\\
&\leqslant C(h^{k+1} + \|\boldsymbol{\xi_p}\| + \|\xi_\rho\|)(\|\boldsymbol{\xi_s}\| + h^{k+1})\\
&\leqslant C(h^{2k+2} + \|\xi_\rho\|^2 + \|\boldsymbol{\xi_p}\|^2) + \epsilon\|\boldsymbol{\xi_s}\|^2,
\end{aligned} \tag{3.13}$$

where in the second step we use the Schwarz inequality, the third step follows from Lemma 3.4, and the fourth one requires Lemmas 3.1 and 3.2. Now we proceed to the estimate of R_{23},

$$\begin{aligned}
R_{23} &\leqslant C(\|\eta_\rho\|_{\Gamma_h} + \|\xi_\rho\|_{\Gamma_h})\|[\xi_\rho]\|_{\Gamma_h}\\
&\leqslant Ch^{\frac{1}{2}}(\|\eta_\rho\|_{\Gamma_h} + \|\xi_\rho\|_{\Gamma_h})(\|\boldsymbol{\xi_s}\| + h^{k+1})\\
&\leqslant C(h^{k+1} + \|\xi_\rho\|)(\|\boldsymbol{\xi_s}\| + h^{k+1})\\
&\leqslant C(h^{2k+2} + \|\xi_\rho\|^2) + \epsilon\|\boldsymbol{\xi_s}\|^2,
\end{aligned} \tag{3.14}$$

where the first step follows from the Schwarz inequality, the second step is based on Lemma 3.4, and the third one requires Lemma 3.2. Plug (3.12)–(3.14) into (3.11) to obtain

$$R_2 \leqslant C(\|\boldsymbol{\xi_p}\|^2 + \|\xi_\rho\|^2 + h^{2k+2}) + \epsilon\|\boldsymbol{\xi}_s\|^2. \tag{3.15}$$

Use Hypotheses 3 and Lemma 3.2 to obtain

$$\begin{aligned}
R_3 &= (\rho - \rho_h, \xi_\rho) - (\rho^2 - \rho_h^2, \xi_\rho)\\
&\leqslant C\|\xi_\rho\|(\|\xi_\rho\| + \|\eta_\rho\|) \leqslant C(\|\xi_\rho\|^2 + h^{2k+2}).
\end{aligned} \tag{3.16}$$

The estimate of R_4 follows from Lemma 3.3, i.e.,

$$R_4 \leqslant Ch^{k+1}\|\rho\|_{k+2}\|\boldsymbol{\xi_s}\| \leqslant Ch^{2k+2} + \epsilon\|\boldsymbol{\xi_s}\|^2. \tag{3.17}$$

Substituting the estimation (3.10), (3.15)–(3.17) into (3.9), we obtain

$$\frac{1}{2}\frac{d\|\xi_\rho\|^2}{dt} + \|\boldsymbol{\xi_s}\|^2 \leqslant C(\|\xi_\rho\|^2 + \|\boldsymbol{\xi_p}\|^2 + h^{2k+2}) + \epsilon\|\boldsymbol{\xi_s}\|^2. \tag{3.18}$$

Integrating the above equation (3.18) with respect to t, we have the first energy inequality

$$\|\xi_\rho\|^2 + \int_0^t \|\boldsymbol{\xi_s}\|^2\, dt \leqslant C\int_0^t (\|\xi_\rho\|^2 + \|\boldsymbol{\xi_p}\|^2)\, dt + Ch^{2k+2}. \tag{3.19}$$

3.5 The second energy inequality

In this subsection, we construct the second energy inequality. Take $\boldsymbol{\theta} = \boldsymbol{\xi_p}$, $\underline{r} = \underline{\xi}_{\underline{u}}$ in (3.7) and (3.8), respectively and use Lemma 2.1 and (3.2) to obtain

$$\left(\frac{\partial \xi_p}{\partial t}, \boldsymbol{\xi}_p\right) + \frac{1}{\mathcal{D}}(\underline{\xi}_{\underline{u}}, \underline{\xi}_{\underline{u}}) =: T_1 + T_2 - T_3 - T4, \tag{3.20}$$

where

$$\begin{aligned}
T_1 &:= (\boldsymbol{\eta_p}_t, \boldsymbol{\xi_p}) + \frac{1}{\mathcal{D}}(\underline{\eta}_{\underline{u}}, \underline{\xi}_{\underline{u}}),\\
T_2 &:= \Gamma((r\rho - 1)\boldsymbol{p} - (r\rho_h - 1)\boldsymbol{p}_h, \boldsymbol{\xi_p}),\\
T_3 &:= \Gamma_2(|\boldsymbol{p}|^2\boldsymbol{p} - |\boldsymbol{p}_h|^2\boldsymbol{p}_h, \boldsymbol{\xi_p}),\\
T_4 &:= \mathcal{K}(\boldsymbol{\eta_p}, \underline{\xi}_{\underline{u}}).
\end{aligned}$$

Now we estimate T_i $(i = 1, 2, 3, 4)$ term by term. Using Hypothesis 3, the Schwartz inequality and Lemma 3.2 we have

$$\begin{aligned}
T_1 &\leqslant C\|\boldsymbol{\xi_p}\|\|\boldsymbol{\eta_p}_t\| + \frac{1}{\mathcal{D}}\|\underline{\xi}_{\underline{u}}\|\|\underline{\eta}_{\underline{u}}\|\\
&\leqslant Ch^{k+1}(\|\boldsymbol{\xi_p}\| + \|\underline{\xi}_{\underline{u}}\|) \leqslant Ch^{2k+2} + C\|\boldsymbol{\xi_p}\|^2 + \epsilon\|\underline{\xi}_{\underline{u}}\|^2.
\end{aligned} \tag{3.21}$$

The estimate of T_2 requires Lemma 3.2, Hypothesis 3 and (3.4),

$$\begin{aligned}
T_2 &= \Gamma(r\rho(\boldsymbol{p} - \boldsymbol{p}_h), \boldsymbol{\xi_p}) + \Gamma(r(\rho - \rho_h)\boldsymbol{p}_h, \boldsymbol{\xi_p}) - \Gamma(\boldsymbol{p} - \boldsymbol{p}_h, \boldsymbol{\xi_p})\\
&\leqslant C\|\boldsymbol{\xi_p}\|(\|\boldsymbol{\xi_p}\| + \|\boldsymbol{\eta_p}\| + \|\xi_\rho\| + \|\eta_\rho\|)\\
&\leqslant C(\|\boldsymbol{\xi_p}\|^2 + \|\xi_\rho\|^2 + h^{2k+2}).
\end{aligned} \tag{3.22}$$

Using Lemma 3.2 and Hypothesis 1, we estimate T_3 through

$$\begin{aligned}
T_3 &= \Gamma_2(|\boldsymbol{p}|^2(\boldsymbol{p} - \boldsymbol{p}_h) + (|\boldsymbol{p}|^2 - |\boldsymbol{p}_h|^2)\boldsymbol{p}_h, \boldsymbol{\xi_p})\\
&= \Gamma_2(|\boldsymbol{p}|^2(\boldsymbol{p} - \boldsymbol{p}_h), \boldsymbol{\xi_p}) + \Gamma_2((|\boldsymbol{p}| + |\boldsymbol{p}_h|)\boldsymbol{p}_h(|\boldsymbol{p}| - |\boldsymbol{p}_h|), \boldsymbol{\xi_p})\\
&\leqslant C\|\boldsymbol{\xi_p}\|(\|\boldsymbol{\xi_p}\| + \|\boldsymbol{\eta_p}\|) \leqslant C(\|\boldsymbol{\xi_p}\|^2 + h^{2k+2}).
\end{aligned} \tag{3.23}$$

Here, we use the fact that $||\boldsymbol{p}| - |\boldsymbol{p}_h|| \leqslant |\boldsymbol{p} - \boldsymbol{p}_h|$, and hence

$$\||\boldsymbol{p}| - |\boldsymbol{p}_h|\| \leqslant \||\boldsymbol{p} - \boldsymbol{p}_h|\| = \|\boldsymbol{p} - \boldsymbol{p}_h\|.$$

For T_4, we use Lemma 3.3 to obtain

$$T_4 \leqslant Ch^{k+1}\|\boldsymbol{p}\|_{k+2}\|\underline{\xi}_{\underline{u}}\| \leqslant Ch^{2k+2} + \epsilon\|\underline{\xi}_{\underline{u}}\|^2. \tag{3.24}$$

Substituting (3.21)–(3.24) into (3.20), we have

$$\frac{1}{2}\frac{d}{dt}\|\boldsymbol{\xi_p}\|^2 + \|\mathcal{D}^{-1/2}\underline{\xi}_{\underline{u}}\|^2 \leqslant C(\|\boldsymbol{\xi_p}\|^2 + \|\xi_\rho\|^2 + h^{2k+2}) + \epsilon\|\underline{\xi}_{\underline{u}}\|^2.$$

By taking ϵ to be small enough and using Hypothesis 1, the above equation leads to

$$\frac{d}{dt}\|\boldsymbol{\xi_p}\|^2 + \|\underline{\xi}_{\underline{u}}\|^2 \leqslant C(\|\boldsymbol{\xi_p}\|^2 + \|\xi_\rho\|^2 + h^{2k+2}).$$

Integrating the above equation with respect to t, we obtain

$$\|\boldsymbol{\xi_p}\|^2 + \int_0^t \|\underline{\xi}_{\underline{u}}\|^2\, dt \leqslant C\int_0^t (\|\boldsymbol{\xi_p}\|^2 + \|\xi_\rho\|^2)\, dt + Ch^{2k+2}. \tag{3.25}$$

3.6 Proof of Theorem 2.2

Now we are ready to combine the two energy inequalities and finish the proof of Theorem 2.2.

Firstly, from (3.19) and (3.25), it is easy to derive the following estimate:

$$\|\xi_\rho\|^2 + \|\boldsymbol{\xi_p}\|^2 + \int_0^t (\|\boldsymbol{\xi_s}\|^2 + \|\underline{\xi}_{\underline{u}}\|^2)dt \leqslant C \int_0^t (\|\boldsymbol{\xi_p}\|^2 + \|\xi_\rho\|^2)\ dt + Ch^{2k+2}.$$

Now, we can employ Gronwall's inequality to obtain

$$\|\xi_\rho\|^2 + \|\boldsymbol{\xi_p}\|^2 + \int_0^t \|\boldsymbol{\xi_s}\|^2 dt + \int_0^t \|\underline{\xi}_{\underline{u}}\|^2\ dt \leqslant Ch^{2k+2}.$$

Finally, by using the standard approximation result, we obtain (2.19). To complete the proof, let us verify the *a priori* assumption (3.3). For $k \geqslant 1$, we can consider h small enough so that $Ch^{k+1} < \frac{1}{2}h$, where C is the constant determined by the final time T. Then define

$$t^* = \inf\{t : \|\rho - \rho_h\| + \|\boldsymbol{p} - \boldsymbol{p}_h\| \geqslant h\}.$$

We should have $\|\rho - \rho_h\| + \|\boldsymbol{p} - \boldsymbol{p}_h\| = h$ by continuity in time at $t = t^*$. However, if $t^* < T$, Theorem 2.2 implies that

$$\|\rho - \rho_h\| + \|\boldsymbol{p} - \boldsymbol{p}_h\| \leqslant Ch^{k+1}$$

for $t \leqslant t^*$, in particular

$$h = \|(\rho - \rho_h)(t^*)\| + \|(\boldsymbol{p} - \boldsymbol{p}_h)(t^*)\| \leqslant Ch^{k+1} < \frac{1}{2}h,$$

which leads to a contradiction. Therefore, there always holds $t^* \geqslant T$, and thus the *a priori* assumption (3.3) is justified.

4 Time discretization

In this section, we give the semi-implicit spectral deferred correction (SDC) time discretization after the LDG discretization of the dynamic model of pattern formation (2.1)–(2.4). More details for the semi-implicit SDC time discretization can be found in [16,21]. The SDC time method, compared with classical SDC time methods, does not require separation of stiff and non-stiff components, which is more general and efficient.

To employ the SDC method, first of all it is necessary to construct a first-order semi-implicit scheme. For the pattern formation dynamical model, the source terms are non-trivial and we treat them in a special way. The corresponding first-order semi-implicit scheme is

$$\frac{\rho^{n+1} - \rho^n}{\Delta t} + \nabla \cdot (\rho^{n+1}\boldsymbol{p}^n) + \nabla \cdot \boldsymbol{s}^{n+1} = \rho^{n+1}(1 - \rho^n), \tag{4.1}$$

$$\boldsymbol{s}^{n+1} + \nabla \rho^{n+1} = 0, \tag{4.2}$$

$$\frac{\boldsymbol{p}^{n+1} - \boldsymbol{p}^n}{\Delta t} + \nabla \cdot \underline{u}^{n+1} - \Gamma(r\rho^{n+1} - 1)\boldsymbol{p}^{n+1} + \Gamma_2|\boldsymbol{p}^n|^2\boldsymbol{p}^{n+1} = 0, \tag{4.3}$$

$$\frac{1}{\mathcal{D}}\underline{u}^{n+1} = -\nabla \boldsymbol{p}^{n+1}. \tag{4.4}$$

One obvious benefit of the first-order semi-implicit scheme (4.1)–(4.4) is that it can be decomposed into two systems: (4.1)–(4.2) for ρ^{n+1} and (4.3)–(4.4) for $\boldsymbol{p}^{n+1}$. Then we can solve the two systems independently. Note that the first-order scheme (4.1)–(4.4) leads to a linear system for $\boldsymbol{U}^{n+1} = (\rho^{n+1}, \boldsymbol{p}^{n+1})^{\mathrm{T}}$. Applying the LDG discretization for the first-order semi-implicit schemes (4.1)–(4.4), we obtain an ODE system

$$\boldsymbol{U}_t^n = \mathcal{F}(t, \boldsymbol{U}^n, \boldsymbol{U}^{n+1}), \quad t \in [0, T],$$

$$\boldsymbol{U}(0) = \boldsymbol{U}_0, \tag{4.5}$$

where $\mathcal{F}$ is continuous for $\boldsymbol{U}$ and t.

Now we construct higher-order SDC time discretization based on the first-order scheme (4.1)–(4.4). Divide the time interval $[t_n, t_{n+1}]$ into P subintervals by choosing the points $t_{n,m}$ for $m = 0, 1, \ldots, P$ such that

$$t_n = t_{n,0} < t_{n,1} < \cdots < t_{n,m} < \cdots < t_{n,p} = t_{n+1}.$$

Let $\Delta t_{n,m} = t_{n,m+1} - t_{n,m}$ and $\boldsymbol{U}_{n,m}^k$ denotes the k-th-order approximation to $u(t_{n,m})$. The points $\{t_{n,m}\}_{m=0}^p$ are chosen to be the Chebyshev Gauss-Lobatto nodes on $[t_n, t_{n+1}]$. Starting from $\boldsymbol{U}_n$, we calculate $\boldsymbol{U}_{n+1}$ in the following algorithm. In Algorithm 1, we denote $I_m^{m+1}(\mathcal{F}(t, \boldsymbol{U}^k, \boldsymbol{U}^k))$ to the integral of the P-th degree interpolating polynomial on the $P+1$ points $\mathcal{F}(t_{n,m}, \boldsymbol{U}_{n,m}^k, \boldsymbol{U}_{n,m}^k)_{m=0}^P$ over the subinterval $[t_{n,m}, t_{n,m+1}]$, which is the numerical quadrature approximation of

$$\int_{t_{n,m}}^{t_{n,m+1}} \mathcal{F}(\tau, \boldsymbol{U}(\tau), \boldsymbol{U}(\tau)) d\tau.$$

The computation of

$$\int_{t_{n,m}}^{t_{n,m+1}} \mathcal{F}(\tau, \boldsymbol{U}(\tau), \boldsymbol{U}(\tau)) d\tau$$

is based on the P-th degree Lagrange interpolation formulation of $\mathcal{F}(\tau, \boldsymbol{U}(\tau), \boldsymbol{U}(\tau))$ on the $P+1$ Gauss type points over the subinterval $[t_{n,m}, t_{n,m+1}]$. The local truncation error obtained with the semi-implicit SDC scheme is $O(\delta t^{\min(K+1, P+1)})$, where $\delta t = \max_{n,m}(t_{n,m})$. For more details of the SDC time discretization, see [16].

Algorithm 1 The SDC time integration method

Require: $\boldsymbol{U}_{n,0}^1 = \boldsymbol{U}_n$;
Use a first-order semi-implicit scheme to compute the approximate solution $\boldsymbol{U}^1$ at the nodes $\{t_{n,m}\}_{m=1}^p$, i.e.,
for $m = 0, 1, \ldots, P-1$ **do**
  $\boldsymbol{U}_{n,m+1}^1 = \boldsymbol{U}_{n,m}^1 + \Delta t_{n,m} \mathcal{F}(t_{n,m}, \boldsymbol{U}_{n,m}^1, \boldsymbol{U}_{n,m+1}^1)$.
end for
Compute successive corrections based on the first-order scheme:
for $k = 1, \ldots, K$ **do**
  $\boldsymbol{U}_{n,0}^{k+1} = \boldsymbol{U}_n$
end for
for $m = 0, 1, \ldots, P-1$ **do**
  $\boldsymbol{U}_{n,m+1}^{k+1} = \boldsymbol{U}_{n,m}^{k+1} + \Delta t_{n,m}(\mathcal{F}(t_{n,m+1}, \boldsymbol{U}_{n,m+1}^k, \boldsymbol{U}_{n,m+1}^{k+1}) - \mathcal{F}(t_{n,m+1}, \boldsymbol{U}_{n,m+1}^k, \boldsymbol{U}_{n,m+1}^k)) + I_m^{m+1}(\mathcal{F}(t, \boldsymbol{U}^k, \boldsymbol{U}^k))$
end for

5 Numerical examples

In this section we provide numerical examples to illustrate the accuracy and capability of the numerical method. The first example is the accuracy test to verify our theoretical analysis, and the rest examples are real problems performed in [13, 18]. The LDG discretization, combined with a semi-implicit SDC integration method, is used to solve (2.5)–(2.8).

Example 5.1. We solve (1.1)–(1.2) and the parameters are taken as

$$\mathcal{D} = 2, \quad r = 1, \quad \Gamma = 10 \quad \text{and} \quad \Gamma_2 = 0.1. \tag{5.1}$$

The exact smooth solutions are given as

$$\rho(\boldsymbol{x}, t) = \mathrm{e}^{\sin(t)} \sin(x) \sin(y), \quad p_1(\boldsymbol{x}, t) = \mathrm{e}^{\sin(t)} \sin(x) \cos(y),$$
$$p_2(\boldsymbol{x}, t) = \mathrm{e}^{\cos(t)} \cos(x) \sin(y).$$

We can calculate the initial conditions and the right-hand sides accordingly.

Piecewise linear and quadratic tensor product polynomials are used in the LDG scheme. We use uniform meshes with $M \times M$ elements over the computational domain $\Omega = [0, 2\pi] \times [0, 2\pi]$, and compute the numerical approximations at $T = 0.2$. Periodic boundary condition is used in this numerical example. The numerical results are given in Table 1. From the table, we can observe optimal convergence rates, which verifies the results in Theorem 2.2.

In the rest several examples, we study the actin pattern formation by the coefficient Γ which is the ratio between alignment and the polymerization rate. Unless otherwise stated, the parameters are taken as

$$\mathcal{D} = 5, \quad r = 1.1 \quad \text{and} \quad \Gamma_2 = 0.075. \tag{5.2}$$

Examples 5.2 and 5.4 were performed by [18] with a characteristic finite element method. When $\Gamma = 4.3$, spirals were caught at high density spots. Example 5.3 was studied in [13] by a finite difference method, where a uniform density profile or waves have been obtained for various values of Γ. We use an LDG spatial discretization combined with the second-order SDC time scheme in the simulations.

Example 5.2. The computational domain is $\Omega = [0, 150]^2$. The initial density and filament polarization of F-action are given by

$$\begin{aligned} &\rho(x, y, 0) = 0.8 + 10^{-4}\text{rand}(0, 1), \\ &p_1(x, y, 0) = 10^{-2}(2\text{rand}(0, 1) - 1), \quad p_2(x, y, 0) = 10^{-2}(2\text{rand}(0, 1) - 1), \end{aligned} \tag{5.3}$$

where rand$(0, 1)$ represents the random number in $[0, 1]$. The parameter Γ in the modelling equations is chosen as $\Gamma = 4.3$.

The computed mesh is composed of 150×150 elements with equal size. The time step in the second-order SDC time scheme is $\Delta t = 0.1$. The contour plots of density of the actin and the vector space for average filament polarization with time evolution are shown in Figure 1. From the figures, we can see that the density of the actin first grow, and align at $\rho = 1$, then several spots with higher density emerge at $t = 40$, and the corresponding filament polarization shows spiral around the spots. At later stage the spots move and disappear, then waves with regular width show up in the end. The results agree with those in [13, 18].

Example 5.3. We study the actin pattern formation by the coefficient Γ with various values. The computational domain is $\Omega = [0, 150]^2$. The initial density and filament polarization of F-action are given by

$$\begin{aligned} &\rho(x, y, 0) = 0.8 + 10^{-4}\text{rand}(0, 1), \\ &p_1(x, y, 0) = 10^{-2}(2\text{rand}(0, 1) - 1), \quad p_2(x, y, 0) = 10^{-2}(2\text{rand}(0, 1) - 1), \end{aligned} \tag{5.4}$$

Table 1 Accuracy test for Example 5.1, the results are solutions at the final time $T = 0.2$ for the LDG discretization with piecewise linear polynomial combined with the second-order SDC time discretization, and quadratic polynomial combined with the third-order SDC time discretization. The time step is $\Delta t = 0.1h$ with $h = \frac{2\pi}{M}$

Mesh	$\|\rho - \rho_h\|_{L^2}$	Order	$\|\rho - \rho_h\|_{L^\infty}$	Order	$\|\boldsymbol{p} - \boldsymbol{p}_h\|_{L^2}$	Order	$\|\boldsymbol{p} - \boldsymbol{p}_h\|_{L^\infty}$	Order
8^2	5.46E−01	–	1.80E−01	–	1.29E−01	–	3.90E−01	–
16^2	1.40E−01	1.96	4.85E−02	1.89	3.35E−01	1.95	1.07E−01	1.87
32^2	3.53E−02	1.99	1.25E−02	1.96	8.48E−02	1.98	2.75E−02	1.96
64^2	8.84E−03	2.00	3.16E−03	1.98	2.12E−02	2.00	6.93E−03	1.99
128^2	2.21E−03	2.00	7.95E−04	1.99	5.31E−03	2.00	1.74E−03	2.00
8^2	7.03E−02	–	3.65E−02	–	1.66E−01	–	7.17E−02	–
16^2	8.89E−03	2.95	4.29E−03	3.09	2.14E−02	2.96	9.15E−03	2.97
32^2	1.12E−03	2.99	5.21E−04	3.04	2.69E−03	2.99	1.13E−03	3.01
64^2	1.40E−04	3.00	6.43E−05	3.01	3.37E−04	3.00	1.41E−04	3.01
128^2	1.75E−05	3.00	7.99E−06	3.00	4.22E−05	3.00	1.74E−05	3.00

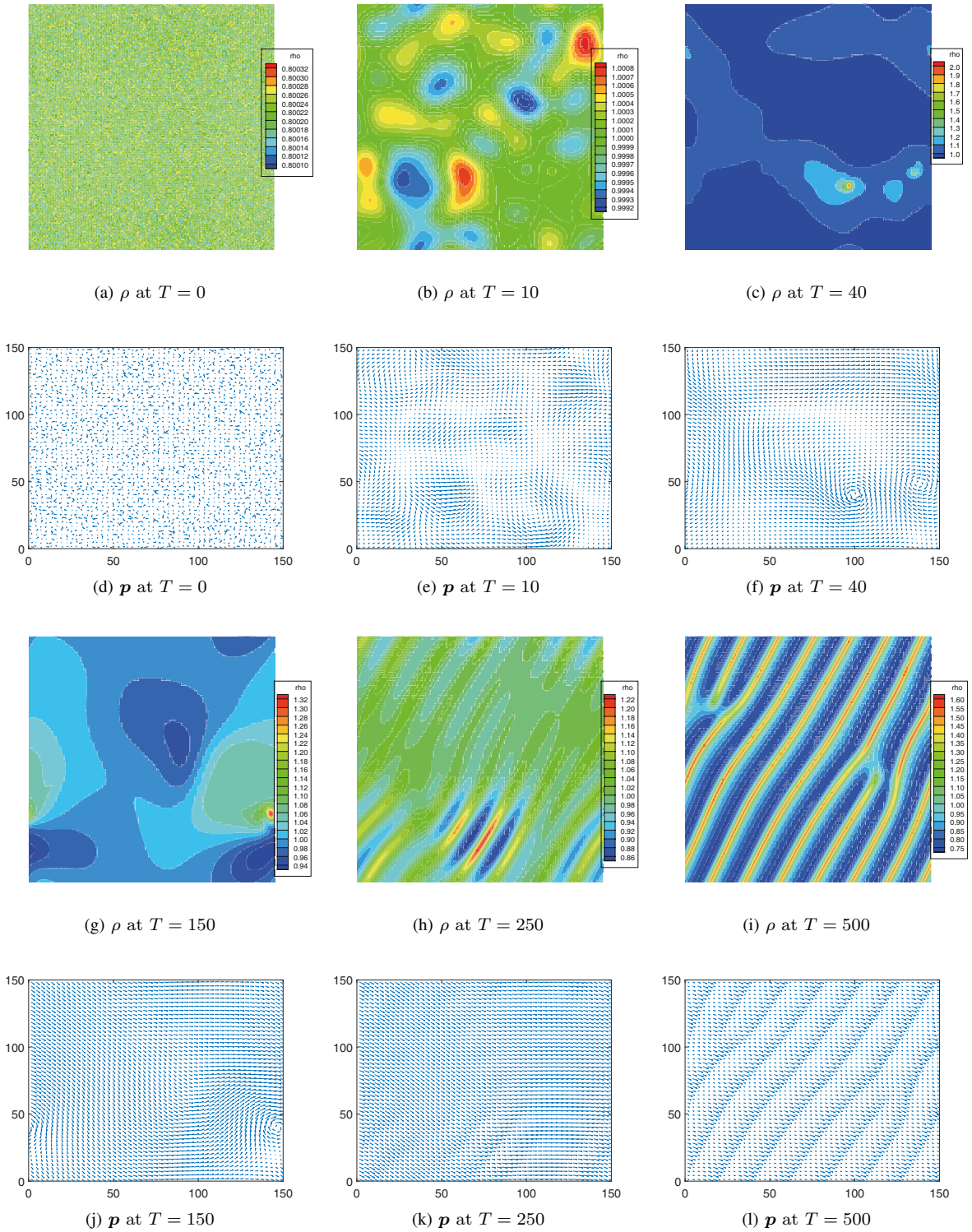

(a) ρ at $T = 0$ (b) ρ at $T = 10$ (c) ρ at $T = 40$

(d) $\boldsymbol{p}$ at $T = 0$ (e) $\boldsymbol{p}$ at $T = 10$ (f) $\boldsymbol{p}$ at $T = 40$

(g) ρ at $T = 150$ (h) ρ at $T = 250$ (i) ρ at $T = 500$

(j) $\boldsymbol{p}$ at $T = 150$ (k) $\boldsymbol{p}$ at $T = 250$ (l) $\boldsymbol{p}$ at $T = 500$

Figure 1 (Color online) Example 5.2, numerical density and filament polarization with time evolution for (1.1)–(1.2) with parameters $\Gamma = 4.3$, $D = 5$, $r = 1.1$ and $\Gamma_2 = 0.075$. Initial conditions are set as (5.4), and the uniform mesh is composed of 150×150 elements with periodic boundary conditions. An LDG discretization with piecewise linear polynomials and a second-order SDC time scheme with time step $\Delta t = 0.1$ are used during the simulation

where rand$(0, 1)$ represents the random number in $[0, 1]$. Various values of Γ are chosen, namely $1, 4.3$ and 10, respectively.

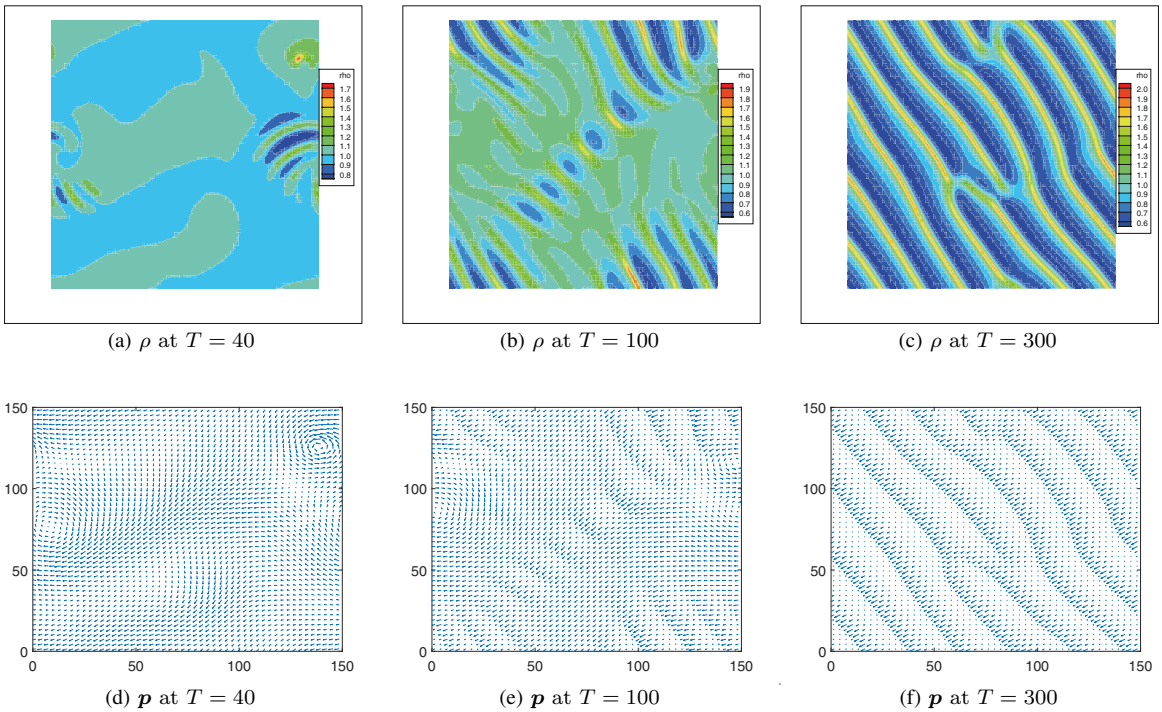

(a) ρ at $T = 40$ (b) ρ at $T = 100$ (c) ρ at $T = 300$

(d) $\boldsymbol{p}$ at $T = 40$ (e) $\boldsymbol{p}$ at $T = 100$ (f) $\boldsymbol{p}$ at $T = 300$

Figure 2 (Color online) Example 5.3, numerical density and filament polarization with time evolution for (1.1)–(1.2) with parameters $D = 5$, $r = 1.1$, $\Gamma_2 = 0.075$ and $\Gamma = 4.3$. Initial conditions are set as (5.5), and the uniform mesh is composed of 100×100 elements with periodic boundary conditions. An LDG discretization with piecewise linear polynomials and a second-order SDC time scheme with time step $\Delta t = 0.1$ are used during the simulation

The computed mesh is composed of 100×100 elements with equal size. Note that the initial conditions in this example are different from those of Example 5.2 since the random numbers are different. The time steps in the second-order SDC time scheme are $\Delta t = 0.1$ for $\Gamma = 1$ and $\Gamma = 4.3$, and $\Delta t = 0.02$ for $\Gamma = 10$. The contour plots of density of the actin and the vector space for average filament polarization at several times are shown in Figure 2 for $\Gamma = 4.3$, and Figure 3 for $\Gamma = 1$ and $\Gamma = 10$. From Figure 2, we can see similar trend for spots, wave formation on a coarse mesh with 100×100 elements. The top two rows of Figure 3 are results for $\Gamma = 1$, showing that the density grows until $\rho = 1.0$ then stays at the stage. The final state in the case of $\Gamma = 1$ is uniform. The bottom two rows of Figure 3 for $\Gamma = 10$ show that the density grows up to $\rho = 1.0$, subsequently high density points emerge, then waves form. Comparing the bottom two rows of Figure 3 for $\Gamma = 10$ with results of Figure 2 for $\Gamma = 4.3$, we can see that in the case of $\Gamma = 10$, the waves start earlier and no spiral shows up around the high density spots. These results confirm the numerical simulations derived by the finite difference method in [13].

Example 5.4. The computational domain is $\Omega = [0, 50]^2$. The initial density and initial filament polarization of F-action are given by

$$\begin{aligned} &\rho(x, y, 0) = 0.4 + 0.4\mathrm{e}^{-20(x-25)^2-20(y-25)^2} 10^{-4}\mathrm{rand}(0, 1), \\ &p_1(x, y, 0) = 10^{-2}(2\mathrm{rand}(0, 1) - 1), \quad p_2(x, y, 0) = 10^{-2}(2\mathrm{rand}(0, 1) - 1), \end{aligned} \tag{5.5}$$

where $\mathrm{rand}(0, 1)$ again represents the random number in $[0, 1]$. We take $\Gamma = 10$.

The computed mesh is composed of 100×100 elements with equal size. The time step in the second-order SDC time scheme is $\Delta t = 0.02$ for $\Gamma = 10$. The contour plots of density of the actin and the vector space for average filament polarization with time evolution are shown in Figure 4. Similar to the results of [18], the density grows until $\rho = 1$, and filament polarization close to $\mathbf{0}$. The solution stay at the stage for a period of time, and waves form in the end.

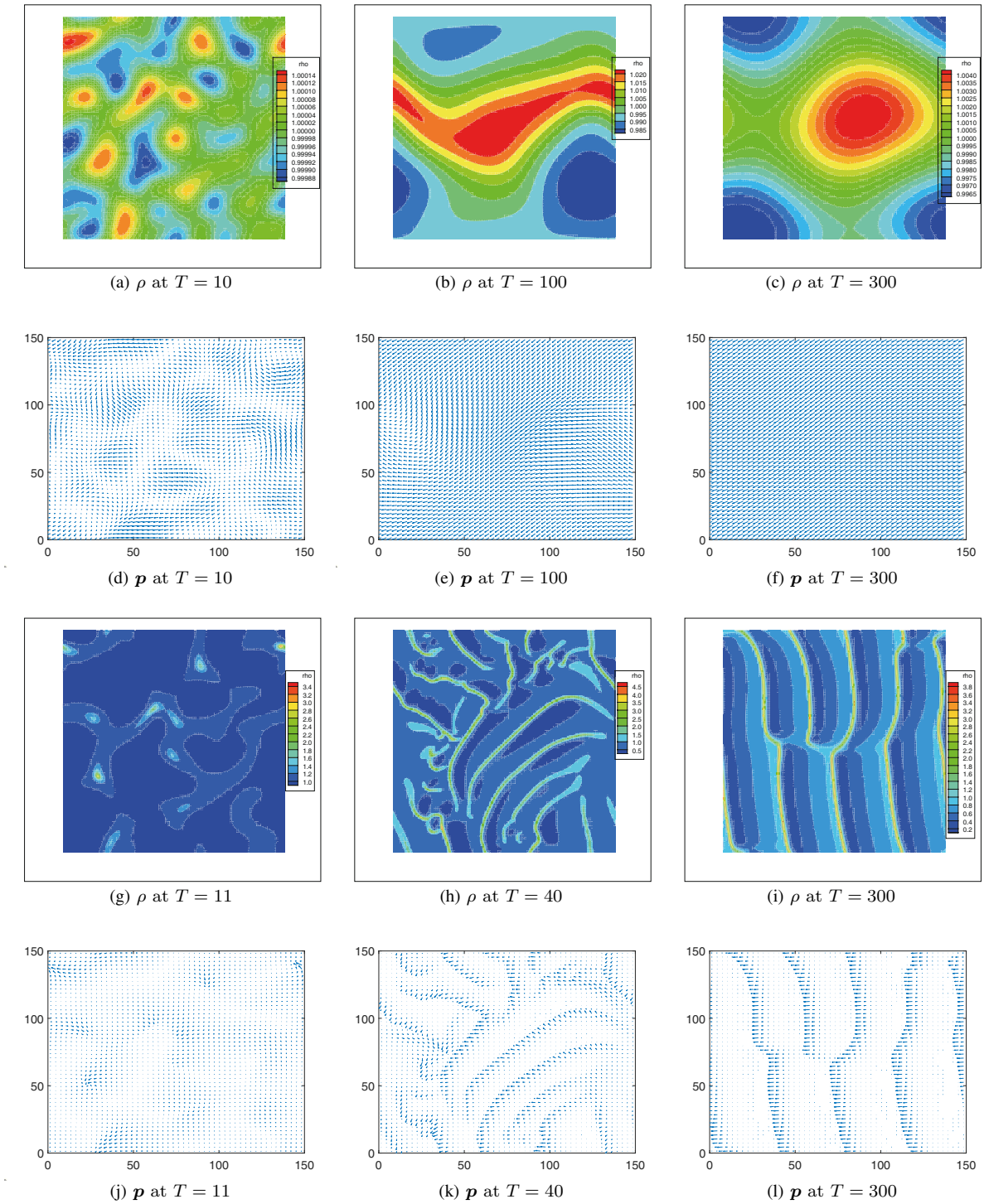

(a) ρ at $T = 10$ (b) ρ at $T = 100$ (c) ρ at $T = 300$

(d) $\boldsymbol{p}$ at $T = 10$ (e) $\boldsymbol{p}$ at $T = 100$ (f) $\boldsymbol{p}$ at $T = 300$

(g) ρ at $T = 11$ (h) ρ at $T = 40$ (i) ρ at $T = 300$

(j) $\boldsymbol{p}$ at $T = 11$ (k) $\boldsymbol{p}$ at $T = 40$ (l) $\boldsymbol{p}$ at $T = 300$

Figure 3 (Color online) Example 5.3, numerical density and filament polarization with time evolution for (1.1)–(1.2) with parameters $D = 5$, $r = 1.1$, $\Gamma_2 = 0.075$. The top two rows of figures are numerical solutions for $\Gamma = 1$ while the bottom two rows for $\Gamma = 10$. Initial conditions are set as (5.5), and the uniform mesh is composed of 100×100 elements with periodic boundary conditions. An LDG discretization with piecewise linear polynomials and a second-order SDC time scheme are used during the simulation

6 Concluding remarks

In this paper, we studied the pattern formation dynamical model in polymerizing action flocks through an LDG method, and optimal convergence rates were derived. Numerical experiments verified the theoretical

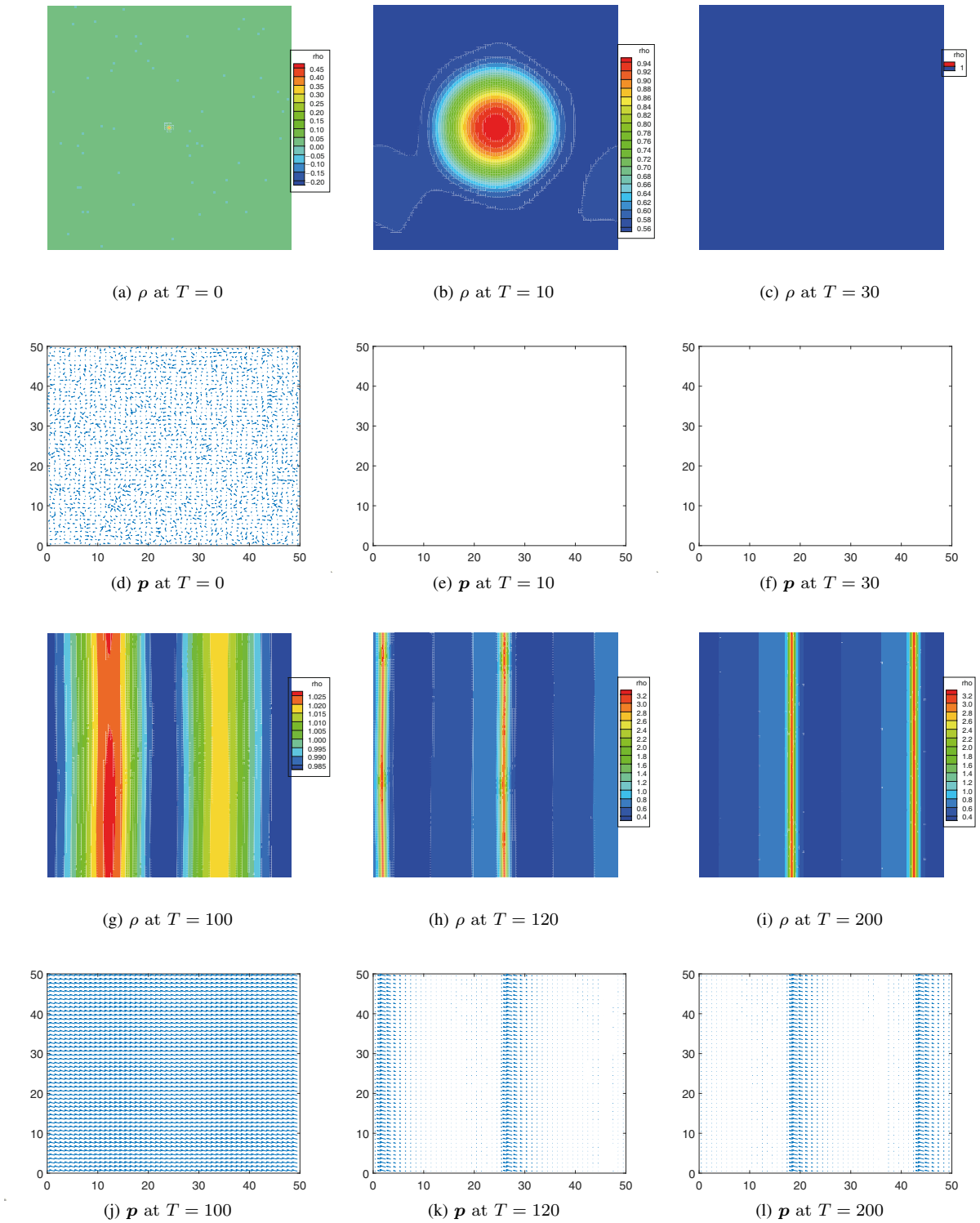

(a) ρ at $T = 0$ (b) ρ at $T = 10$ (c) ρ at $T = 30$

(d) $\boldsymbol{p}$ at $T = 0$ (e) $\boldsymbol{p}$ at $T = 10$ (f) $\boldsymbol{p}$ at $T = 30$

(g) ρ at $T = 100$ (h) ρ at $T = 120$ (i) ρ at $T = 200$

(j) $\boldsymbol{p}$ at $T = 100$ (k) $\boldsymbol{p}$ at $T = 120$ (l) $\boldsymbol{p}$ at $T = 200$

Figure 4 (Color online) Example 5.4, numerical density and filament polarization with time evolution for (1.1)–(1.2) with parameters $D = 5$, $r = 1.1$, $\Gamma_2 = 0.075$ and $\Gamma = 10$. Initial conditions are set as (5.6), and the uniform mesh is composed of 100×100 elements with periodic boundary conditions. An LDG discretization with piecewise linear polynomials and a second-order SDC time scheme are used during the simulation

analysis and capabilities of the LDG method. In particular, we caught spiral around a spot in actin pattern formation simulations for a suitable ratio between the change rate of the direction of F-action

filaments and the polymerization rate. We will consider positivity of the density for the explicit Runge-Kutta time method. The physical and numerical energy of the model and the adaptive strategy in long time simulations will also be explored in the future.

Acknowledgements This work was supported by National Natural Science Foundation of China (Grant Nos. 11801569 and 11571367), Natural Science Foundation of Shandong Province (CN) (Grant Nos. ZR2018BA011 and ZR2019MA015), the Fundamental Research Funds for the Central Universities (Grant Nos. 18CX02021A and 18CX05003A) and National Science Foundation of USA (Grant No. DMS-1818467).

References

1 Bassi F, Rebay S. A high-order accurate discontinuous finite element method for the numerical solution of the compressible Navier-Stokes equations. J Comput Phys, 1997, 131: 267–279
2 Castillo P, Cockburn B, Perugia I, et al. Superconvergence of the local discontinuous Galerkin method for elliptic problems on cartesian grids. SIAM J Numer Anal, 2001, 39: 264–285
3 Ciarlet P. The Finite Element Method for Elliptic Problems. Amsterdam-New York: North-Holland, 1978
4 Cockburn B, Hou S, Shu C-W. The Runge-Kutta local projection discontinuous Galerkin finite element method for conservation laws. IV: The multidimensional case. Math Comp, 1990, 54: 545–581
5 Cockburn B, Kanschat D, Schötzau D. A locally conservative LDG method for the incompressible Navier-Stokes equations. Math Comp, 2005, 74: 1067–1095
6 Cockburn B, Lin S Y, Shu C-W. TVB Runge-Kutta local projection discontinuous Galerkin finite element method for conservation laws. III: One-dimensional systems. J Comput Phys, 1989, 84: 90–113
7 Cockburn B, Shu C-W. TVB Runge-Kutta local projection discontinuous Galerkin finite element method for conservation laws. II: General framework. Math Comp, 1989, 52: 411–435
8 Cockburn B, Shu C-W. The Runge-Kutta discontinuous Galerkin method for conservation laws. V: Multidimensional systems. J Comput Phys, 1998, 141: 199–224
9 Cockburn B, Shu C-W. The local discontinuous Galerkin method for time-dependent convection-diffusion systems. SIAM J Numer Anal, 1998, 35: 2440–2463
10 Cross M-C, Hohenberg P-C. Pattern formation outside of equilibrium. Rev Modern Phys, 1993, 65: 851–1112
11 Dutt A, Greengard L, Rikhlin V. Spectral deferred correction methods for ordinary differential equations. BIT, 2000, 40: 241–266
12 Feng X, Tang T, Yang J. Long time numerical simulations for phase-field problems using p-adaptive spectral deferred correction methods. SIAM J Sci Comput, 2015, 37: A271–A294
13 Goff T-L, Liebchen B, Marenduzzo D. Pattern formation in polymerizing actin flocks: Spirals, spots, and waves without nonlinear chemistry. Phys Rev Lett, 2016, 117: 238002
14 Gollub J-P, Langer J-S. Pattern formation in nonequilibrium physics. Rev Modern Phys, 1999, 71: S396–S403
15 Guo H, Tian L, Xu Z Y, et al. High-order local discontinuous Galerkin method for simulating wormhole propagation. J Comput Appl Math, 2019, 350: 247–261
16 Guo R, Xia Y, Xu Y. Semi-implicit spectral deferred correction methods for highly nonlinear partial differential equations. J Comput Phys, 2017, 338: 269–284
17 Guo R, Xu Y. Local discontinuous Galerkin method and high order semi-implicit scheme for the phase field crystal equation. SIAM J Sci Comput, 2016, 38: A105–A127
18 Jiang M S, Zhang J S, Zhu J, et al. Characteristic finite element analysis of pattern formation dynamical model in polymerizing actin flocks. Appl Math Lett, 2019, 98: 224–232
19 Li X, Shu C-W, Yang Y. Local discontinuous Galerkin method for the Keller-Segel chemotaxis model. J Sci Comput, 2017, 73: 943–967
20 Liu F, Shen J. Stabilized semi-implicit spectral deferred correction methods for Allen-Cahn and Cahn-Hilliard equations. Math Methods Appl Sci, 2015, 38: 4564–4575
21 Minion M. Semi-implicit spectral deferred correction methods for ordinary differential equations. Commun Math Sci, 2003, 1: 471–500
22 Reed W-H, Hill T-R. Triangular mesh method for the neutron transport equation. Technical Report LA-UR-73-479. Los Alamos: Los Alamos Scientific Laboratory, https://www.osti.gov/servlets/purl/4491151, 1973
23 Tang T, Xie H, Yin X. High-order convergence of spectral deferred correction methods on general quadrature nodes. J Sci Comput, 2012, 56: 1–13
24 Wang H, Wang S, Zhang Q, et al. Local discontinuous Galerkin methods with implicit-explicit time marching for multi-dimensional convection diffusion problems. ESAIM: M2AN, 2016, 50: 1083–1105
25 Wang H J, Liu Y, Zhang Q, et al. Local discontinuous Galerkin methods with implicit-explicit time-marching for

time-dependent incompressible fluid flow. Math Comp, 2018, 315: 91–121
26 Wang H J, Shu C-W, Zhang Q. Stability and error estimates of local discontinuous Galerkin methods with implicit-explicit time-marching for advection-diffusion problems. SIAM J Numer Anal, 2015, 53: 206–227
27 Wang H J, Shu C-W, Zhang Q. Stability analysis and error estimates of local discontinuous Galerkin methods with implicit-explicit time-marching for nonlinear convection-diffusion problems. Appl Math Comput, 2016, 272: 237–258
28 Xu Y, Shu C-W. Error estimates of the semi-discrete local discontinuous Galerkin method for nonlinear convection-diffusion and KdV equations. Comput Methods Appl Mech Engrg, 2007, 196: 3805–3822
29 Xu Y, Shu C-W. Local discontinuous Galerkin methods for high-order time-dependent partial differential equations. Commun Comput Phys, 2010, 7: 1–46
30 Yan J, Shu C-W. Local discontinuous Galerkin methods for partial differential equations with higher order derivatives. J Sci Comput, 2002, 17: 27–47
31 Yan J, Shu C-W. A local discontinuous Galerkin method for KdV type equations. SIAM J Numer Anal, 2002, 40: 769–791
32 Yang Y, Shu C-W. Analysis of sharp superconvergence of local discontinuous Galerkin method for one-dimensional linear parabolic equations. J Comput Math, 2015, 33: 323–340